MNRAS **000**, 1–12 (0000) Preprint 10 December 2019 Compiled using MNRAS LATEX style file v3.0

The first high-redshift changing-look quasars

Nicholas P. Ross[1]★, Matthew J. Graham[2], Giorgio Calderone[3], K. E. Saavik Ford[4,5,6], Barry McKernan[4,5,6] and Daniel Stern[7]

[1]*Institute for Astronomy, University of Edinburgh, Royal Observatory, Blackford Hill, Edinburgh EH9 3HJ, United Kingdom*
[2]*Cahill Center for Astronomy and Astrophysics, California Institute of Technology, Mail Code 249/17, 1200 E California Blvd, Pasadena CA 91125, USA*
[3]*INAF – Osservatorio Astronomico di Trieste, Via Tiepolo 11, I-34143 Trieste, Italy*
[4]*Department of Science, BMCC, City University of New York, New York, NY 10007, USA*
[5]*Department of Astrophysics, Rose Center for Earth and Space, American Museum of Natural History, Central Park West at 79th Street, NY 10024, USA*
[6]*Graduate Center, City University of New York, 365 5th Avenue, New York, NY 10016, USA*
[7]*Jet Propulsion Laboratory, California Institute of Technology, 4800 Oak Grove Drive, Mail Stop 169-221, Pasadena, CA 91109, USA*

Accepted XXX. Received YYY; in original form ZZZ

ABSTRACT

We report on three redshift $z > 2$ quasars with dramatic changes in their C IV emission lines, the first sample of changing-look quasars (CLQs) at high redshift. This is also the first time the changing-look behaviour has been seen in a high-ionisation emission line. SDSS J1205+3422, J1638+2827, and J2228+2201 show interesting behaviour in their observed optical light curves, and subsequent spectroscopy shows significant changes in the C IV broad emission line, with both line collapse and emergence being displayed in rest-frame timescales of ∼240-1640 days. These are rapid changes, especially when considering virial black hole mass estimates have all three quasars with $M_{\rm BH} > 10^9 M_\odot$. Continuum and emission line measurements from the three quasars show changes in the continuum-equivalent width plane with the CLQs seen to be on the edge of the full population distribution, and showing indications of an intrinsic Baldwin effect. We put these observations in context with recent state-change models, but note that even in their low-state, the C IV CLQs are above ∼10% in Eddington luminosity.

Key words: accretion, accretion discs – surveys – quasars: general – quasars: time-domain:

1 INTRODUCTION

Luminous AGN, i.e. quasars, are now seen to significantly vary their energy output on timescales as short as weeks to months. This observation, and the subsequent mismatch in the expected "viscous" timescale, which for a 10^7 $M_\odot$ central supermassive black hole (SMBH) is ∼hundreds of years, was noted over 30 years ago (e.g. Alloin et al. 1985). However, with new photometric light-curve and repeat spectroscopic data, the desire for a deeper understanding of AGN accretion disk physics has recently re-invigorated the field (e.g. Antonucci 2018; Lawrence 2018; Ross et al. 2018; Stern et al. 2018).

The optical continuum variability of quasars has been recognized since their first optical identification (e.g., Matthews & Sandage 1963). Dramatic changes in the broad emission lines (BELs) of quasars has only recently been identified (e.g., LaMassa et al. 2015). Samples of over 100 "changing-look" quasars (CLQs) or "changing-state" quasars (CSQs) have now been assembled (e.g., MacLeod et al. 2019; Graham et al. 2019a). The community uses both these terms as a cover for the underlying physics. For sake of argument, CLQs can potentially be thought of as the extension to the BELs of quasar continuum variability (e.g., MacLeod et al. 2012) whereas the CSQs have a state-transition similar to that in Galactic X-ray binaries (Noda & Done 2018; Ruan et al. 2019). In this paper, we use the term "changing-look", as we are currently agnostic, and confessedly ignorant, to the underlying physical processes.

CLQs to date have primarily been defined according to the (recombination) Balmer emission line properties with particular attention paid to the Hβ emission line, observed from optical spectroscopy. Recent works report on discoveries of Mg II changing-look AGN (Guo et al. 2019; Homan et al. 2019). However, current CLQ studies have primarily been at redshifts $z < 1$.

While there have been many studies on triply ionised carbon, i.e., C IV, these have tended to focus on broad absorption line quasars (e.g., Table 1 of Hemler et al. 2019) or the Baldwin effect (Baldwin 1977; Bian et al. 2012; Jensen et al. 2016; Hamann et al. 2017)[1].

[1] As noted in Rakić et al. (2017), two different types of Baldwin effect are present in the literature: *(i)* the *global* (or *ensemble*) Baldwin effect, which is an anti-correlation between the equivalent width of the emission line and the underlying continuum luminosity of *single-epoch* observations of a *large number* of AGN, and *(ii)* the *intrinsic* Baldwin effect, the same anti-correlation but in an *individual, variable* AGN (Pogge & Peterson 1992).

★ E-mail: npross@roe.ac.uk

© 0000 The Authors

Line	λ / Å	Transition Energy / eV	Ionisation Energy / eV	Transition Levels Lower			Upper			Wavenumber / cm^{-1}	$A_{i,j}$ / 10^8 s^{-1}
H LyLim	912.324	13.5984	13.5984	$1s$	^{2}S	1/2	∞			109 678.7	1.23×10^{-6}
H Lyα	1215.670	10.1988	13.5984	$1s$	^{2}S	1/2	2			82 259.2	4.67
N v	1238.821	10.0082	97.8901	$1s^22s$	^{2}S	1/2	$1s^22p$	^{2}P^o	3/2	80 721.9	3.40
N v	1242.804	9.9762	97.8901	$1s^22s$	^{2}S	1/2	$1s^22p$	^{2}P^o	1/2	80 463.2	3.37
C iv	1548.187	8.0083	64.4935	$1s^22s$	^{2}S	1/2	$1s^22p$	^{2}P^o	3/2	64 591.7	2.65
C iv	1550.772	7.9950	64.4935	$1s^22s$	^{2}S	1/2	$1s^22p$	^{2}P^o	1/2	64 484.0	2.64
He ii	1640.474	7.5578	54.4178	$2p$	^{2}P^o	3/2	$3d$	^{2}D	5/2	60 958.0	10.35
He ii	1640.490	7.5578	54.4178	$2p$	^{2}P^o	3/2	$3d$	^{2}D	3/2	60 957.4	1.73
C iii]	1906.683	6.5026	47.8878	$1s^22s^2$	^{1}S	0	$1s^22s2p$	^{3}P^o	2	52 447.1	5.19×10^{-11}
C iii]	1908.734	6.4956	47.8878	$1s^22s^2$	^{1}S	0	$1s^22s2p$	^{3}P^o	1	52 390.8	1.14×10^{-6}
Mg ii	2795.528	4.4338	15.0353	$2p^63s$	^{2}S	1/2	$2p^63p$	^{2}P^o	3/2	35 760.9	2.60
Mg ii	2802.705	4.4224	15.0353	$2p^63s$	^{2}S	1/2	$2p^63p$	^{2}P^o	1/2	35 669.3	2.57
H Ba β	4861.333	2.5497	13.5984	2			4			20 564.8	0.0842

Table 1. Strong UV/optical spectral emission lines in quasars, and their atomic data. Data from the NIST Atomic Spectra Database (Kramida et al. 2018; Kramida et al. 2019). The transition energies are $E = hc/\lambda$ for the given wavelength. The ionisation energy is the energy required to ionise the given species, e.g., 64.49 eV is needed to create a C v ion. Transitions level configurations are given in standard spectroscopic notation, with $A_{i,j}$ denoting the transition probabilities.

Dramatic changes in the collisionally excited broad *emission* line of C iv — and indeed C iii] — have not to this point been reported.

Here, we present new results for three quasars which show dramatic changes in their C iv and C iii] broad emission line properties and underlying continuum. These are some of the first examples of CLQs at high ($z > 1$) redshift. Moreover, these are the first cases for substantial changes of ions with high ionisation potentials (I.P.'s >2 Rydberg), thus linking the ionizing photons to the energetic inner accretion disk.

Details of the atomic transitions that produce strong rest-frame UV/optical lines in quasars are given in Table 1. In this paper we use the wavelengths of 1548.202 and 1550.774 Å for the C iv doublet (Kramida et al. 2018). For ionisation energies, 47.89 eV (3.519 Ry) is required for doubly-ionised C iii to become triply-ionised C iv, and 64.49 eV (4.74 Ry) is needed to ionise C iv itself. This energy corresponds to a thermal temperature of $T \gtrsim 4\times10^5$ K, implying a heating energy source of (soft) X-ray photons.

Wilhite et al. (2006) examine C iv variability in a sample of 105 quasars observed at multiple epochs by the Sloan Digital Sky Survey (SDSS; York et al. 2000; Stoughton et al. 2002; Abazajian et al. 2009a). They find a strong correlation between the change in the C iv line flux and the change in the line width, but no correlations between the change in flux and changes in line center or skewness. These authors find that the relation between line flux change and line width change is consistent with a model in which a broad line base varies with greater amplitude than the line core. The C iv lines in these high-luminosity quasars appear to be less responsive to continuum variations than those in lower luminosity AGN.

Richards et al. (2011) explored the broad emission line region in over 30,000 $z > 1.54$ SDSS quasars, concentrating on the properties of the C iv emission line. These authors consider two well-known effects involving the C iv emission line: *(i)* the anti-correlation between the C iv equivalent widths (EWs) and luminosity (i.e., the Baldwin effect) and *(ii)* the blueshifting of the peak of C iv emission with respect to the systemic redshift. We denote the velocity offset of emission lines as $V_{\rm off}$ and use the convention that a positive $V_{\rm off}$ value means the line is blueshifted while a negative $V_{\rm off}$ value means the line is redshifted. Richards et al. (2011) find a blueshift of the C iv emission line is nearly ubiquitous, with a mean shift of $V_{\rm off}$ ~810 km s^{-1} for radio-quiet (RQ) quasars and $V_{\rm off}$ ~360 km s^{-1} for radio-loud (RL) objects. Richards et al. (2011) also find the Baldwin effect is present in both the RQ and RL studied samples. These author conclude that these two C iv parameters (EW and blueshift) are capturing an important trade-off between "disk" and "wind" components in the disk-wind model of accretion disks (e.g., Murray et al. 1995; Elvis 2000; Proga et al. 2000; Leighly 2004), with one dominating over the other depending on the shape of the quasar spectral energy distribution (SED).

Using the multi-epoch spectra of 362 quasars from the SDSS Reverberation Mapping project (SDSS-RM; Shen et al. 2015, 2019), Sun et al. (2018) investigate the blueshift of C iv emission relative to Mg ii emission, and its dependence on quasar properties. These authors confirm that high-blueshift sources tend to have low C iv EWs, and that the low-EW sources span a range of blueshift. Other high-ionisation lines, such as He ii , also show similar blueshift properties. The ratio of the line width of C iv to that of Mg ii increases with blueshift. Sun et al. (2018) also find that quasar variability might slightly enhance the connection between the C iv blueshift and EW, though further investigation here is warranted. They also find that quasars with the largest blueshifts are less variable and tend to have higher Eddington ratios. Eddington ratio alone might be an insufficient condition for the C iv blueshift. Recent investigations also include Meyer et al. (2019) and Doan et al. (2019). Dyer et al. (2019) provide a detailed analysis of 340 quasars at high redshift ($1.62 < z < 3.30$) from the SDSS-RM project, which we compare our results to in Section 4.2.

The purpose of this paper is, for the first time, to systematically access and report on the CLQ phenomenon at high ($z > 2$) redshift. While accessing this phenomenon at an earlier cosmic epoch is somewhat interesting, the main value of this study is we move from the low-ionisation energy Balmer emission line series to the high-ionisation emission lines, in particular C iv λ1549.

This paper is organised as follows. In Section 2, we describe our sample selection, catalogues, and observational data sets. Section 3 presents the high-redshift quasars and reports their time-variable line properties. We provide a brief theoretical discussion in Section 4, and Section 5 presents our conclusions. We report all magnitudes on the AB zero-point system (Oke & Gunn 1983; Fukugita et al. 1996) unless otherwise stated. For the WISE bands, $m_{\rm AB} = m_{\rm Vega} + m$ where $m = (2.699, 3.339)$ for *WISE* W1 (3.4μm) and W2 (4.6μm), respectively (Cutri et al. 2011; Cutri 2013). We adopt a flat ΛCDM cosmology with $\Omega_\Lambda = 0.73$, $\Omega_{\rm M} = 0.27$, and $h = 0.71$. All logarithms are to the base 10.

Object	Redshift	g-band / mag	MJD	Instrument	Exposure time / sec	SDSS Plate-FiberID	Notes
	2.068	18.27	53498	SDSS	8057	2089-427	
J120544.7+342252.4	2.071		58538	DBSP	1800	—	Average conditions
	2.071		58693	DBSP	2400	—	
	2.185	19.77	54553	SDSS	4801	2948-614	
J163852.9+282707.7	2.186		55832	BOSS	3600	5201-178	
	2.182		58583	LRIS	1800	—	
	2.217	19.97	56189	BOSS	2700	6118-720	
J222818.7+220102.9	2.222		56960	BOSS	4500	7582-790	eBOSS reobservation
	2.222		58693	DBSP	2400	—	

Table 2. Details of our spectroscopic observations. Redshift errors are typically ±0.002. SDSS, BOSS and eBOSS spectra have $\mathcal{R}$ ~2,000. DBSP: Double Spectrograph on the Palomar 200-inch telescope. LRIS: Low Resolution Imaging Spectrometer on Keck I 10m telescope.

2 DATA, CLQ SELECTION AND LINE MEASUREMENTS

In this section we present the photometric data used to select the CLQs, and then give details to the multiwavelength data where we have it. We then give details of the spectroscopic data including emission lines measurements.

2.1 Photometry

2.1.1 Optical Photometry

We use optical data from the Catalina Real-time Transient Survey (CRTS; Drake et al. 2009; Mahabal et al. 2011), the Panoramic Survey Telescope and Rapid Response System (PanSTARRS; Kaiser et al. 2010; Stubbs et al. 2010; Tonry et al. 2012; Magnier et al. 2013) and the Zwicky Transient Facility (ZTF; Bellm et al. 2019a).

The CRTS archive[2] contains the Catalina Sky Survey data streams from three telescopes – the 0.7 m Catalina Sky Survey (CSS) Schmidt and 1.5 m Mount Lemmon Survey (MLS) telescopes in Arizona and the 0.5 m Siding Springs Survey (SSS) Schmidt in Australia. CRTS covers up to ~2500 deg^2 per night, with 4 exposures per visit, separated by 10 min. The survey observes over 21 nights per lunation. The data are broadly calibrated to Johnson V (see Drake et al. 2013, for details) and the current CRTS data set contains time series for approximately 400 million sources to $V \sim 20$ above Dec > -30 from 2003 to 2016 May (observed with CSS and MLS) and 100 million sources to $V \sim 19$ in the southern sky from 2005 to 2013 (from SSS). CRTS has been used to study distant quasars previously (Graham et al. 2014, 2015a,b, 2017, 2019a).

PanSTARRS data is obtained via the Pan-STARRS Catalog Search interface[3]. We query the PS1 DR2 Detection catalog.

The ZTF is a new robotic time-domain sky survey capable of visiting the entire visible sky north of -30 deg. declination every night. ZTF observes the sky in the g, r, and i-bands at different cadences depending on the scientific program and sky region (Bellm et al. 2019b; Graham et al. 2019b). The ZTF 576 megapixel camera with a 47 deg^2 field of view, installed on the Samuel Oschin 48-inch Schmidt Telescope, can scan more than 3750 deg^2 per hour, to a 5σ detection limit of 20.7 mag in the r-band with a 30sec exposure during new moon (Masci et al. 2019).

[2] http://catalinadata.org
[3] https://catalogs.mast.stsci.edu/panstarrs/

2.1.2 Multi-Wavelength Properties

Mid-infrared data (3.4 and 4.6μm) is available from the beginning of the *Wide-field Infrared Survey Explorer* (*WISE*) mission (2010 January; Wright et al. 2010) through the fifth-year of *NEOWISE-R* operations (2018 December; Mainzer et al. 2011). The *WISE*WISE scan pattern leads to coverage of the full-sky approximately once every six months (a "sky pass"), but the satellite was placed in hibernation in 2011 February and then reactivated in 2013 October. Hence, our light curves have a cadence of 6 months with a 32-month sampling gap.

2.2 CLQ Selection

Our high-z CLQs were identified as follows. We selected all 64,774 SDSS DR15 sources with $z > 0.35$ classified as 'quasar', having at least two spectra separated by at least 100 days, and with a corresponding CRTS light curve. We fitted a damped random walk to the CRTS data via Gaussian process regression and the photometric magnitudes at the epochs of the SDSS spectra for a given source are predicted. Those where $|\Delta V| > 0.3$ are then selected for visual inspection. Only three quasars SDSS J120544.7+342252.4 (hereafter J1205+3422), SDSS J163852.93+282707.7 (hereafter J1638+2827) and SDSS J222818.76+220102.9 (hereafter J2228+2201), satisfied these selection criteria and showed interesting or dramatic emission line behaviour.

2.3 Spectroscopy

An overview of our spectroscopic observations is given in Table 2. The spectra are from the SDSS (Stoughton et al. 2002; Abazajian et al. 2009b; Schneider et al. 2010), the SDSS-III Baryon Oscillation Spectroscopic Survey (BOSS; Eisenstein et al. 2011; Dawson et al. 2013; Smee et al. 2013; Alam et al. 2015; Pâris et al. 2017) and the SDSS-IV Extended Baryon Oscillation Spectroscopic Survey (eBOSS; Dawson et al. 2016; Abolfathi et al. 2018; Pâris et al. 2018). These quasars were targetted via a range of techniques and algorithms (see Richards et al. 2002; Ross et al. 2012; Myers et al. 2015). The SDSS, BOSS, and eBOSS data are supplemented by spectra from the Low Resolution Imaging Spectrometer (LRIS; Oke et al. 1995) on the 10m Keck I telescope. and the Double Spectrograph (DBSP) instrument on the 200" Palomar telescope.

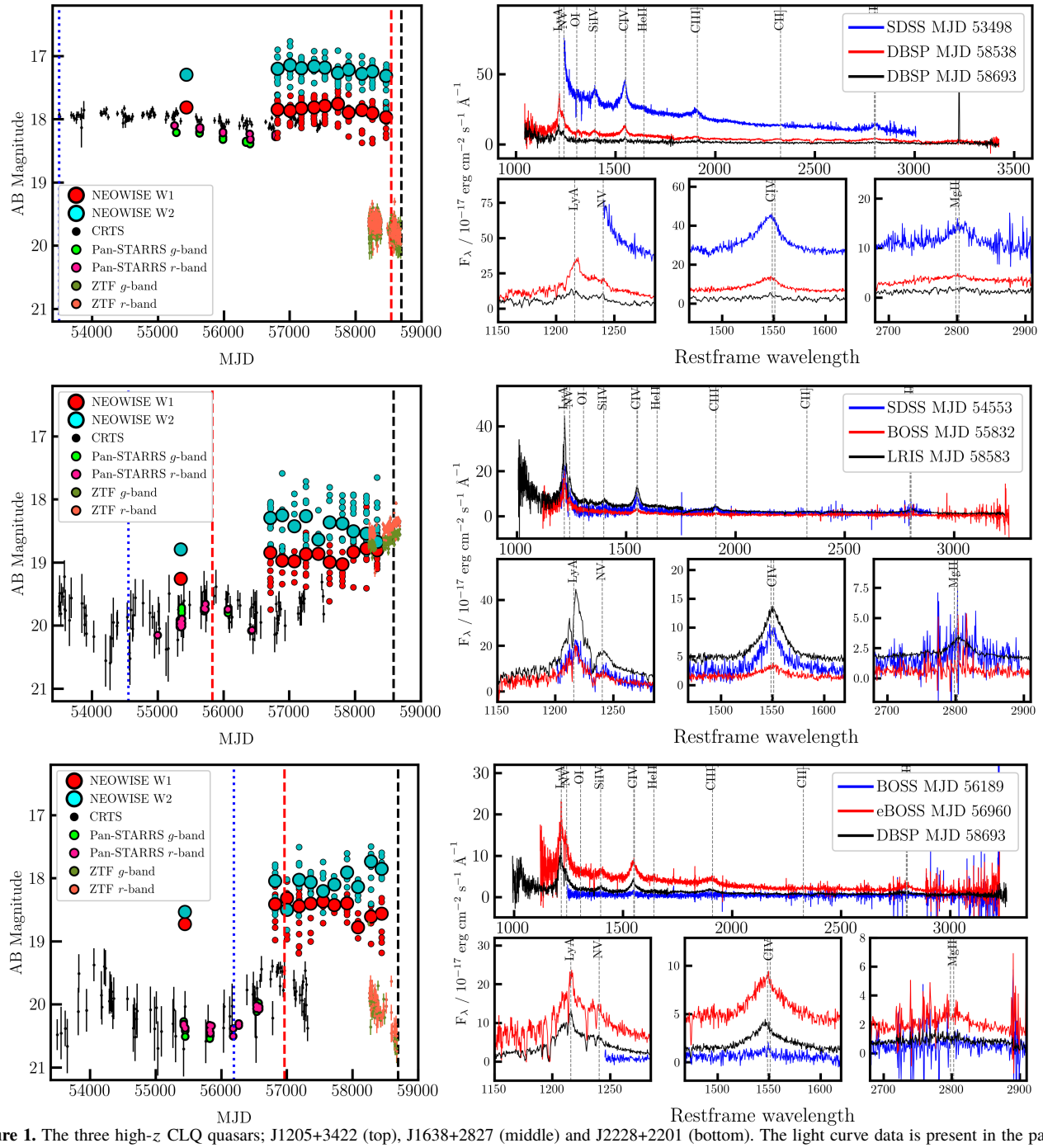

Figure 1. The three high-z CLQ quasars; J1205+3422 (top), J1638+2827 (middle) and J2228+2201 (bottom). The light curve data is present in the panels on the left hand side, with the spectral epoch observational timings indicated by vertical lines. The spectra are on the right hand side, with zoom-in's on the Lyα-N v complex, the C iv line, and the Mg ii line.

2.3.1 Spectrophotometry

We want all our spectra to have reliable flux calibrations. SDSS spectra ae spectrophotometrically calibrated. BOSS and eBOSS spectra have spectrophotometric corrections applied in the latest data release (Hutchinson et al. 2016; Jensen et al. 2016; Margala et al. 2016). Due to the high-z of our objects, [O iii] is not available to us to use as a calibrating flux line. Instead we use photometric data from the ZTF since all our non-SDSS/BOSS/eBOSS data are taken after MJD 57500.

2.4 Emission Line and Power-law Slope Measurements

We use the measured quasar emission line properties from several catalogues: Shen et al. (2011), Hamann et al. (2017), Kozłowski (2017), and Calderone et al. (2017).

In particular we use the Quasar Spectral Fitting (QSFit) software package presented in Calderone et al. (2017). This provides luminosity estimates as well as width, velocity offset and equivalent width of 20 emission lines, including C iv, C iii] and Mg ii . We process and fit all nine spectra using the lastest version (v1.3.0) of the QSFit online calculator. The host galaxy and blended iron emission

Object	MJD	Cont. @ 1450Å νL_ν 10^{42} erg s^{-1}	Slope ($F_\lambda \propto \lambda^\alpha$)	Luminosity 10^{42} erg s^{-1}	CIV 1549Å FWHM km s^{-1}	V_{off} km s^{-1}	EW Å	Virial product $\log(\nu L_\nu^{0.5} \times \mathrm{FWHM}^2)$ $\log(M/M_\odot)$
	53498	38129 ± 39	-1.57 ± 0.01	898 ± 15	6024 ± 120	944 ± 33	37.78 ± 0.62	9.85 ± 0.02
J1205+3422	58538	8550 ± 11	-1.41 ± 0.01	385.2 ± 3.9	7109 ± 91	1085 ± 29	71.32 ± 0.71	9.67 ± 0.01
	58693*	2725 ± 40	-1.27 ± 0.05	161 ± 22	14997 ± 2500	922 ± 690	91.68 ± 12.73	10.07 ± 0.13
	54553	3579 ± 49	-1.16 ± 0.07	293.6 ± 8.8	4630 ± 180	183 ± 57	127.67 ± 3.80	9.11 ± 0.04
J1638+2827	55832	2340 ± 15	-2.17 ± 0.05	84.6 ± 4.2	4733 ± 290	172 ± 89	59.61 ± 2.98	9.04 ± 0.05
	58583	7793 ± 19	-2.02 ± 0.01	367.5 ± 4.3	4511 ± 71	94 ± 24	77.89 ± 0.91	9.25 ± 0.01
	56189*	607 ± 49	-0.00 ± 0.16	72.8 ± 11.3	14993 ± 2400	828 ± 691	162.89 ± 25.37	9.74 ± 0.14
J2228+2201	56960	7842 ± 25	-1.72 ± 0.02	301.0 ± 7.2	7136 ± 210	-276 ± 64	61.99 ± 1.48	9.65 ± 0.03
	58693	2388.4 ± 6.8	-1.22 ± 0.01	145.4 ± 1.5	6084 ± 83	168 ± 28	94.77 ± 0.99	9.26 ± 0.01

Table 3. Continuum at 1450Å and C IV spectral measurements for the three quasar considered in this work, at all observation epochs, as calculated by QSFit. *The C IV line is very faint (with respect to the continuum), and the associated estimates are likely unreliable. For the emission-line velocity offsets, a positive value means the line is blueshifted. The last column shows the virial product calculated as $\nu L_\nu^{0.5} \times \mathrm{FWHM}^2$.

at rest-frame optical wavelengths components are automatically disabled when they can not be constrained by the available data, such as the case for all our objects (we do not have infrared spectral data). Power-law continuum slopes, α, where $f_\lambda \propto \lambda^\alpha$, are also reported in these catalogues and from QSFit.

3 RESULTS

3.1 Photometric and Overall Spectral Evolution

Figure 1 presents the optical and mid-IR light curves for three high-z CLQ quasars. Figure 1 also shows the spectra for each epoch, with the MJD of observation given by the dashed vertical lines in the light curves.

For J1205+3422, our spectral observations cover 5195 days observed, 1691 days in the rest-frame. This quasar was initially identified in SDSS in 2005 May, as a bright, $g \approx 18.0$, blue-sloped quasar with broad Si IV, C IV, C III] and Mg II. C III] and C IV have large blueshifts of ≈2600±150 and ≈1150±100 km s^{-1}, respectively. By 2019, however, the optical brightness dropped by ∼1.5 magnitudes and the spectra are significantly less blue. While Lyα and N V are detectable in both 2019 spectra, C IV has all but disappeared in the 2019 June spectrum. The broad C III] emission has disappeared between the 2005 and 2019 spectra. The changes in C IV and C III] going from broad emission to barely detectable have on the timescales of ≈50 days in the rest-frame.

For J1638+2827, our spectral observations cover 4030 days observed, 1265 days in the rest-frame. Here, in the initial epoch spectrum, C IV is broad and bright, as is C III. However, ≈400 rest-frame days later, the broad C IV and C III] BEL have faded, the continuum slope around 1400Å has changed from ≈ -1.48 to ≈ -2.25, but the Lyα /N V emission complex is very similar in shape and line flux intensity. Around 870 days in the rest-frame after the second spectral epoch, Lyα, N V, C IV, C III] and Mg II are all apparent and broad, with Mg II being seen for the first time at high signal-to-noise. The light curve is consistent with this spectral brightening, increasing from ∼20th magnitude to ∼18.5th magnitude at optical wavelengths. An absorption feature between Lyα and N V is seen in all three spectral epochs.

For J2228+2201, our spectral observations cover 2504 days observed, 778 days in the rest-frame. Over the course of 240 rest-frame days, C IV and C III] both *emerge* as BELs and the standard UV/blue continuum slope increases in flux. Then, over the course of 538 days in the rest-frame, the broadline emission, while still very present, reduces in line flux the UV/blue continuum diminishes, though is still more luminous than the initial BOSS spectrum.

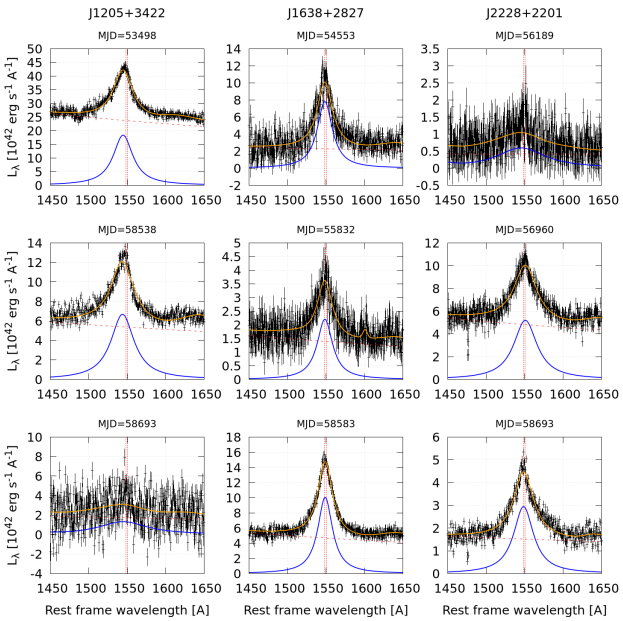

Figure 2. Observed spectra and best fit model in the region relevant to C IV emission line for the quasars considered here. The solid blue line is the Lorentzian profile fit the to the C IV emission line. The long-dashed red line is the continuum fit, with the solid orange line giving the overall fit. The short-dashed vertical lines gives the rest wavelengths of the C IV doublet.

3.2 C IV Emission Line Evolution

We analyzed the spectra of the three quasars, at all observational epochs, using the QSFit spectral fitting package (Calderone et al. 2017). One advantage of using QSFit is that it allows constraints on the slope and luminosity of the broad band continuum of the source. The relevant estimated quantities, including continuum luminosity and slope at rest-frame 1450Å, C IV line luminosity, FWHM and EW are given in Table 3. All fits are performed with $E(B-V) = 0$ and the best fit model in the region of the C IV emission line are shown in Figure 2.

All C IV lines are fitted with a single, broad, Lorentzian profile. This allows us to account for the narrow peak of the C IV line. No narrow components are considered for several reasons: in the epochs of highest brightness the "narrow" component would have FWHM $\sim 2-3\times10^3$ km s^{-1}, i.e. values exceeding the usual widths of genuine narrow lines ($\lesssim 10^3$ km s^{-1}); by allowing a second component, to have such large widths their parameters would become highly degenerate with the "broad" components, and the latter would also have much larger FWHM ($\sim 10^4$ km s^{-1}); moreover, by neglecting the narrow components, we have a consistent model across all epochs.

Both the quasar continuum (evaluated at 1450Å), and the C IV line luminosities follow a similar evolution, with a ratio of ~20-30, confirming that the main driver for emission line variability is likely the broad band continuum itself. For all sources except J1638+2827, the slope of the continuum changes with luminosity following a "bluer-when-brighter" pattern, suggesting that a distinct emerging component is responsible for both the slope and luminosity variations. In J1638+2827 the opposite behaviour is observed, especially in the first observation epoch. However, this may be a bias due to the limited wavelength range available which extends to $\lambda \sim 1240$Å for the first epoch, while it extend to shorter wavelengths for the other epochs (respectively 1140Å and 1010Å). The latter suggests that the "emerging" component is more prominent at UV wavelengths, and a sufficient wavelength coverage is required to detect it. We find there is no need for a narrow component in J2228+2201 MJD 56189. This is because the data resemble a P-Cygni profile, with blueshifted absorption. This feature is very narrow, and the uncertainties large, such that the overall χ^2 is only marginally affected by the addition of a further component. We therefore avoid using a narrow component for this spectrum only, since that would be inconsistent with the other analyses. In all cases where the C IV line profile is reliably constrained and the C IV FWHM is approximately constant, with maximum variations $\lesssim$ 1000 km s^{-1}, despite the significantly larger variations in the line luminosities.

3.3 Virial Black Hole Masses

The FWHM of broad lines is likely related to the mass of the supermassive black hole powering the quasar phenomenon, which is assumed to be constant on any human timescale. Hence it is instructive to check whether the virial product, which is the basic quantity used to calculate the single epoch black hole mass estimate, show any variation.

Using the estimates for the continuum luminosity and FWHW from the single-epoch spectra, one can estimate the central black hole mass (e.g. Shen et al. 2011; Calderone et al. 2017). This approach assumes that the broad-line region (BLR) is virialized, the continuum luminosity is used as a proxy for the BLR radius, and the broad line width (FWHM) is used as a proxy for the virial velocity. This "virial mass" estimate can then be expressed as:

$$\log(M_{\rm BH}) = (\nu L_\nu)^\gamma \times ({\rm FWHM})^\delta \quad (1)$$

where $\gamma = 0.5$ and $\delta = 2$. The virial product for the C IV CLQs is reported in the last column of Tab. 3. The uncertainty typically associated to the single epoch mass estimate is ~0.5 dex, hence the virial product at all epochs are remarkably constant and compatible with a single value of black hole mass for each source, even in those cases where the C IV estimates are possibly unreliable. The object showing larger variation is J2228+2201, although the extreme values span a range of 0.48 dex.

Shen et al. (2011) reports Virial BH mass based on Mg II and C IV as $\log(M_{\rm BH,Vir}/M_\odot) = 9.55 \pm 0.05$ and $\log(M_{\rm BH,Vir}/M_\odot) = 9.49 \pm 0.04$, respectively. We thus use the mean of these five values (three from our three epochs and the two Shen et al. (2011) values) to establish a working mean SMBH mass of $\log(M_{\rm BM,vir}/M_\odot) = 9.726$ for J1205+3422. J1638+2827 also has two virial mass measurments from Shen2011, but also has two measurements from Kozłowski (2017) (again using C IVand Mg II). The mean mass measurement for J1638+2827 here is $\log(M_{\rm BM,vir}/M_\odot = 9.091$. For J2228+2201 there are two Kozłowski (2017), leading to a mean mass of $\log(M_{\rm BM,vir}/M_\odot = 9.366$. We use these mean SMBH masses when calculating the Eddington ratios.

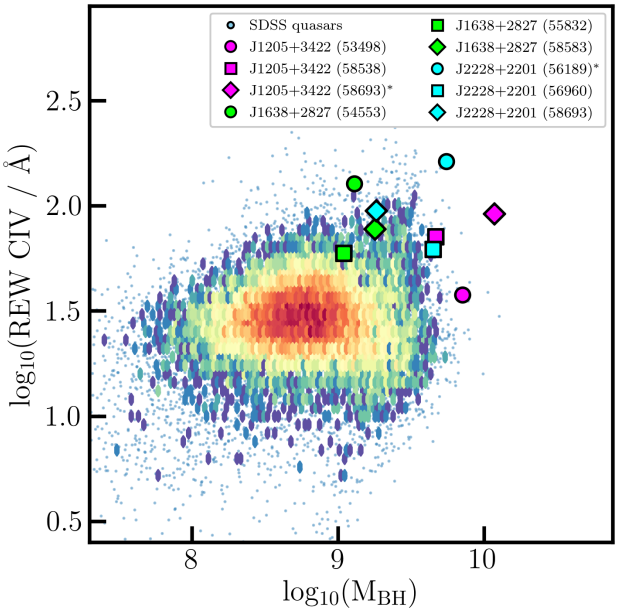

Figure 3. The virial black hole masses of ≈20,000 $z > 1.5$ quasars from QSFit catalogue (Calderone et al. 2017) and the C IV Equivalent widths. Different quasars are given different colours: J1205+3422 purple; J1638+2827 green; J2228+2201 is blue. Different epochs different symbols: first epoch circles; second epoch squares; third epoch diamonds. As noted in Table 3, * signifies the C IV line is very weak and the associated estimates are likely unreliable.

From the virial mass estimates, all our objects have SMBH masses $M > 10^9 M_\odot$. This is at the upper end of SMBH masses at all epochs, and towards the extreme of the mass distribution for $z \sim 2$ objects. Figure 3 shows the C IV Equivalent width and the virial black hole masses for a sample of ≈20,000 $z > 1.5$ SDSS quasars from the QSFit catalog as well as the estimates for the three C IV CLQs.

3.4 Quantified Temporal Evolution of C IV Emission

Quasars with interesting physical properties, such as extreme outflows, can be selected using EW and FWHM measurements, (e.g., the "Extremely Red Quasars" (ERQs) Ross et al. 2015; Zakamska et al. 2016; Hamann et al. 2017; Zakamska et al. 2019). Figure 4 shows the rest Equivalent Width (REW) versus the Full Width Half Maximum (FWHM) of the C IV emission line in the BOSS DR12 quasar sample using the catalogue of Hamann et al. (2017).

The velocity offsets of the C IV line are also approximately constant, and compatible with a single value (within 3σ). The exception is J2228+2201, where a significant change ($\sim 7\sigma$) is observed between the second and third observation epochs. The magnitude of

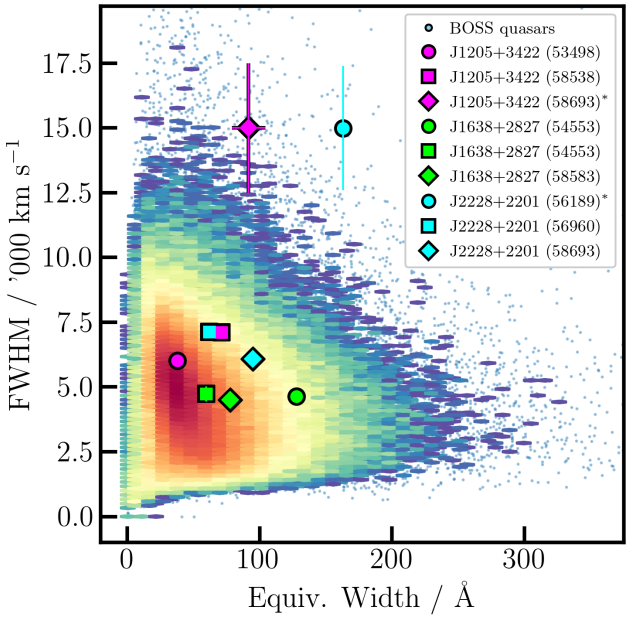

Figure 4. The Rest Equivalent Width (REW) vs. Full Width Half Maximum (FWHM) of the C IV emission line in the BOSS DR12 quasar sample using the catalogue of Hamann et al. (2017). Symbols as in Fig. 3.

Object	MJD	$L_{\rm bol}$	$\eta_{\rm Edd}$
	53498	47.216	-0.610
J1205+3422	58538	46.567	-1.259
	58693	46.070	-1.756
	54553	46.166	-1.025
J1638+2827	55832	45.981	-1.210
	58583	46.504	-0.687
	56189	46.231	-1.235
J2228+2201	56960	47.342	-0.124
	58693	46.826	-0.640

Table 4. Bolometric luminosities are given in either Shen et al. (2011) or Kozłowski (2017) for the three CLQs. We scale these values using our measured νL_ν continuum luminosity values. From Section 3.3, we assume: $\log(M_{\rm BM,vir}/M_\odot) = 9.726$ for J1205+3422; $\log(M_{\rm BM,vir}/M_\odot = 9.091$ for J1638+2827, and $\log(M_{\rm BM,vir}/M_\odot = 9.366$ for J2228+2201. The Eddington Luminosity is $L_{\rm Edd} = 1.26\times10^{38}(M/M_\odot)$ erg s^{-1} and $\eta_{\rm Edd}$ is the log of the Eddington ratio.

the velocity blueshifts ($\sim 200-1100$ km s^{-1}) are consistent with recent results into the properties of rest-frame UV spectra over the redshift range $1.5 \le z \le 7.5$ (Meyer et al. 2019).

The temporal evolution of the velocity offsets, along with the 1450Å continuum luminosity and slope, the C IV line FWHM and virial black hole mass are shown in Figure 5.

3.5 The C IV Baldwin Effect

The Baldwin effect (Baldwin 1977) is an empirical relation between emission-line REWs and continuum luminosity in quasars (Shields 2007; Hamann et al. 2017; Calderone et al. 2017). Hamann et al. (2017) and Calderone et al. (2017) present recent measurements of the Baldwin effect for large quasar samples.

There is an anti-correlation between the emission-line REWs and e.g. 1450Å rest continuum luminosity, so that as the underlying UV continuum luminosity increases, the EW decreases. Figure 6 shows this for a sample (from the QSFit catalogue) for 20,374 quasars. The slope (not shown) is β is -0.1997. This is consistent with Kozłowski (2017), using their bolometric luminosity gives a slope of $\beta = -0.251$ and in line with that from Hamann et al. (2017, $\beta = -0.23$).

We add the measurements from the three C IV CLQ quasars at each epoch to Figure 6. We see first that all three quasars at all three epochs lie on the edge of the νL_ν-EW distribution. Second, with the exception of J1638+2827 on MJD 55832, all the measurements show an *intrinsic Baldwin Effect* (e.g. Goad et al. 2004; Rakić et al. 2017). The slope of the CLQs intrinsic Baldwin effect is ≈ -0.38, as shown by the dashed red line in Fig. 6.

4 DISCUSSION

4.1 Continuum and Line Changes: Comparisons to recent Observations

The top row of Figure 5 demonstrates that both the 1450Å continuum and the C IV emission lines can exhibit large, >×10, changes in luminosity, *and* that these continuum-line changes track each other.

Trakhtenbrot et al. (2019) report on the quasar 1ES 1927+654 which was initially seen to lack broad emission lines and line-of-sight obscuration, i.e, a "Type 2" quasar at redshift $z = 0.02$. This object is then seen to spectroscopically change with the appearance of a blue, featureless continuum, followed by the emergence of broad Balmer emission lines. i.e. this quasar changes into a broad-line Type 1 after a raise in the continuum luminosity. This suggests that there is (at least in some cases) a direct relationship between the continuum and broad emission lines in CLQs. A similar scenario may have occured for the 3 high-z quasars presented here, although we lack the high-cadence multiwavelength, multi-epoch coverage that Trakhtenbrot et al. (2019) present. The multiwavelength data that Trakhtenbrot et al. (2019) includes a UV spectrum of 1ES 1927+654. Interestingly, however, there is no evidence for broad UV emission lines, including C IV, C III, or Mg II. The authors attribute the lack of broad UV emission lines to dust within the BLR, noting that to dust in the broadline emission region, noting that the continuum emission does not show any signs of dust extinction.

MacLeod et al. (2019) present a sample of CLQs where the primary selection requires large-amplitude ($|\Delta g| > 1$ mag, $|\Delta r| > 0.5$ mag) variability over any of the available time baselines probed by the SDSS and Pan-STARRS1 surveys. They find 17 new CLQs which is ~20% of the observed sample. This CLQ fraction increases from 10% to roughly half, as the continuum flux ratio between repeat spectra at 3420 Å (rest-frame) increases from 1.5 to 6. MacLeod et al. (2019) note that these candidates are at lower Eddington ratio relative to the overall quasar population.

Using the same dataset as and extremely variable quasar sample as MacLeod et al. (2019), Homan et al. (2019) investigate the responsiveness of the Mg II broad emission line doublet in AGN on timescales of several years. By again focussing on quasars that show large changes in their optical light-curves, Homan et al. (2019) find that Mg II clearly does respond to the continuum. However, a key finding from Homan et al. (2019) is that the degree of responsivity varies strikingly from one object to another. There are cases of Mg II changing by as much as the continuum, more than the continuum, or very little at all. In the majority (72%) of this highly variable sample, the behaviour of Mg II corresponds with that of Hβ. However, there are also examples of Mg II showing variation, but Hβ does not, and vice versa.

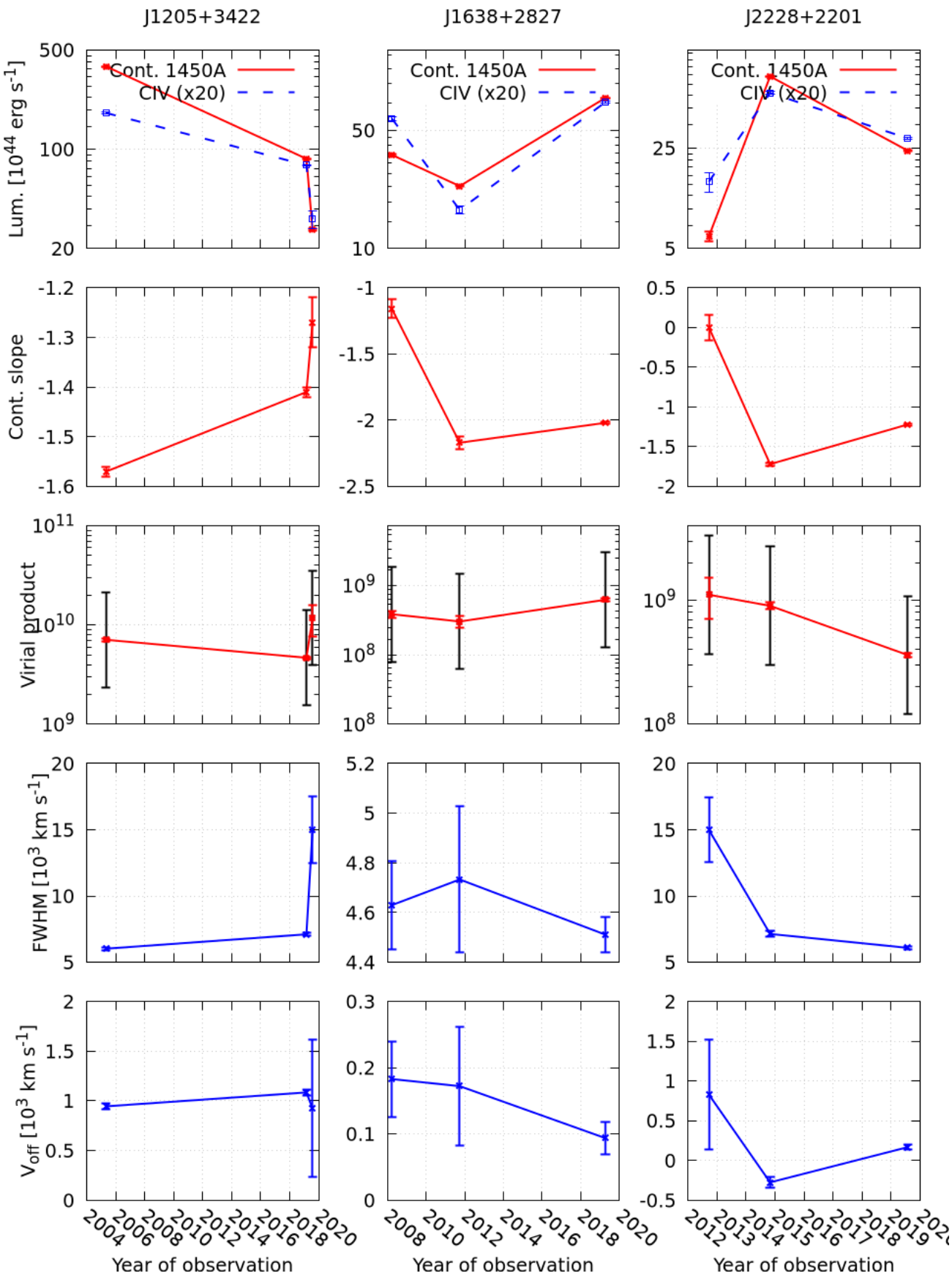

Figure 5. Temporal evolution of the spectral properties of the three quasar considered in this work.

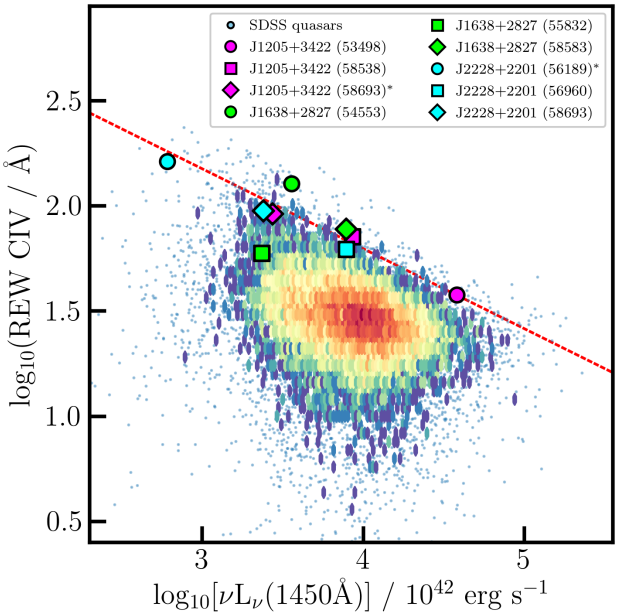

Figure 6. The C IV Equivalent width and the underlying continuum luminosity, commonly referred to as The Baldwin Plot. The continuum luminosities are from Calderone et al. (2017), the REW measurements are Table 3. Symbols as in Fig. 3. The dashed red line has slope $\beta = -0.38$.

Graham et al. (2019a) report the largest number of Hβ CSQs with 111 sources being identified. Graham et al. (2019a) find that this population of extreme varying quasars is associated with *changes* in the Eddington ratio, (rather than just the magnitude of the Eddington ratio itself) and the timescales imply cooling/heating fronts propagating through the disk.

4.2 Continuum and Line Changes: Comparisons to theoretical expectaions

The C IV line is one of the strongest collisionally excited lines in quasar spectra (e.g. Hamann & Ferland 1999), and C IV emission probes the photoionisation environment produced by the innermost disk, as indicated by RM time-delay measurements.

In standard Shakura & Sunyaev (1973) thin disk models, large changes in the continuum flux are not permitted over short timescales due to the relatively long viscous time associated with such disks. Given the observed short timescale continuum variations, we must consider more complex models. We note that two of our sources (J1205+3422 and J2228+2201) have C IV REW and continuum luminosity changes which fall comfortably along a line, implying their variation is consistent with an intrinsic Baldwin Effect (see Fig. 6). That is, the excitation of the C IV line is driven by the changes in the continuum; however the excited gas cannot reach an equilibrium excitation state as quickly as the continuum changes, thus the slope of the intrinsic Baldwin Effect line is greater than that of the overall (ensemble) slope, which is derived from many single-epoch observations, the majority of which are assumed to be in equilibrium.

The presence of an intrinsic Baldwin Effect implies those sources may comfortably fit into the sample of C IV variable quasars explored by Dyer et al. (2019). Similar to those authors, we consider slim accretion disk models e.g., Abramowicz et al. (1988) which may explain the observed variability. In particular, we note the summary timescales for disk variation in Stern et al. (2018), which are shorter for taller disks, permitting changes similar to those observed if they are caused by heating or cooling fronts propagating on the disk sound crossing time. Dyer et al. (2019) also consider inhomogeneous disk models (e.g. Dexter & Agol 2011) where flux variations are driven by azimuthal inhomogeneities in the temperature of the disk. Such inhomogeneities could arise from disk instabilities (e.g. Lightman & Eardley 1974) or interactions of embedded objects (e.g. McKernan et al. 2014, 2018). If an inhomogeneous disk is responsible for the continuum variations, which then drive C IV variations, it implies that our objects are simply the extreme outliers produced by a process which rarely but occasionally produces very large hot or cool spots. The frequency of such occurrences can be used to constrain the slope and normalization of the power law distribution of spot size.

Finally, we must also consider the disk/wind model which has successfully reproduced many features of quasar C IV observations, notably the common blueshifted offset (see e.g., Murray et al. 1995). In this model C IV is very optically thick at low velocities, but optically thin at high velocity, with $\tau \sim 1$ at ~5000 km s^{-1}. In a disk wind model, the broad line region is very small, implying short-timescales of variability in the lines. Also in this model, there should be associated strong absorption in the soft X-ray band, which can be tested with follow-up observations with Chandra.

The foregoing discussion directly applies to the two objects which maintain an intrinsic Baldwin Effect relationship between C IV REW and continuum luminosity. However, J1638+2827 clearly does not maintain such a relationship–indeed the continuum and C IV REW are at least somewhat correlated, rather than anti-correlated in this source. This implies that the illumination of the C IV emitting region by a variable ionizing continuum and the corresponding change in the photoionisation state alone cannot explain the collapse and recovery of the line.

4.3 Eddington Ratios and State Changes

The broad UV and optical lines in quasars are most sensitive to the extreme ultraviolet (EUV) part of the spectral energy distribution (SED), with C IV (and indeed He II and N V) being at the higher energy end of the EUV distribution.

The soft X-ray excess – the excess of X-rays below 2 keV with respect to the extrapolation of the hard X-ray spectral continuum model – is Noda & Done (2018) note that The soft X-ray excess produces most of the ionizing photons, so its dramatic drop leads to the disappearance of the broad-line region, driving the "changing-look" phenomena. major difference is that radiation pressure should be much more important in AGNs, so that the sound speed is much faster than expected from the gas temperature. This spectral hardening appears similar to the soft-to-hard state transition in black hole binaries at $L/L_{\rm Edd} \sim 0.02$ (i.e. $\eta_{\rm Edd} \sim -1.7$), where the inner disc evaporates into an advection dominated accretion flow, while the overall drop in luminosity appears consistent with the hydrogen ionisation disc instability. Crucially Noda & Done (2018) make the prediction that all changing-look AGNs are similarly associated with the state transition at $L/L_{\rm Edd}$ ~a few per cent.

By comparing the observed correlations between the UV/optical-to-X-ray spectral index ($\alpha_{\rm ox}$) and Eddington ratio in AGN to those predicted from observations of X-ray binary outbursts, Ruan et al. (2019) find a remarkable similarity to accretion state transitions in prototypical X-ray binary outbursts, including an inversion of this correlation at a critical Eddington ratio of ~10^{-2}

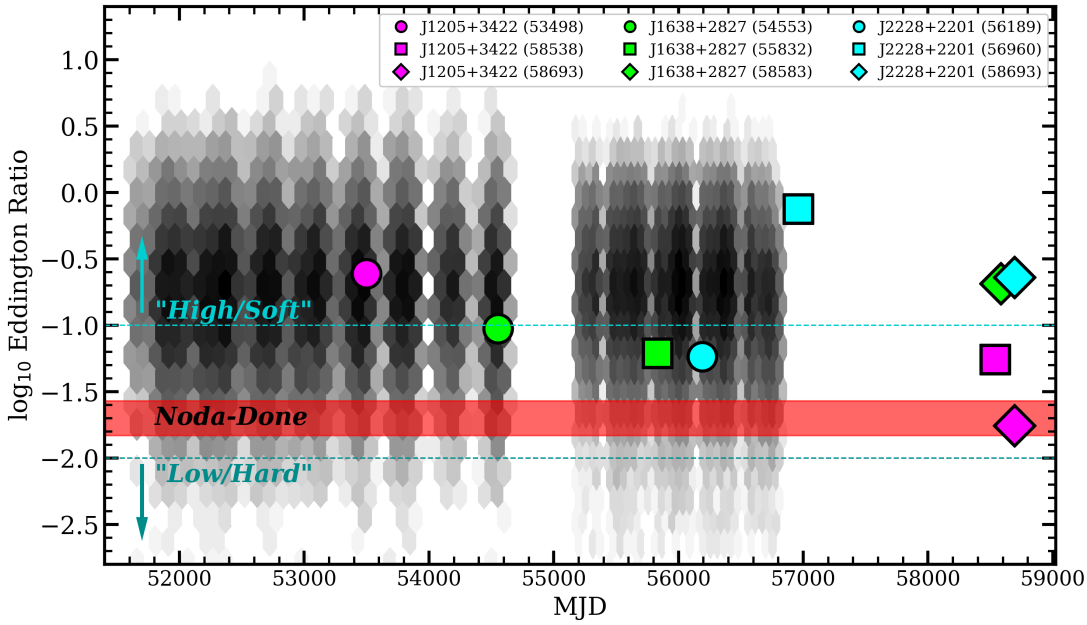

Figure 7. Eddington Ratios of the three C IV CLQs. Grayscale gives the Eddington Ratio ranges for the SDSS (from Shen et al. 2011) and the BOSS (from Kozłowski 2017) catalogues. Symbols as in Fig. 3. The red region ($L/L_{\rm Edd} \approx 0.02 \pm 0.01$; $\eta = -1.7 \pm 0.13$) is the transition accretion rate suggested by Noda & Done (2018). A "High/Soft State" with $\eta_{\rm Edd} \geq -1$ and a a "Low/Hard State" with $\eta_{\rm Edd} \leq -2$ are indicated with dahsed lines and arrows.

(i.e. at the same ratio as motivated by Noda & Done (2018)). These results suggest that the structures of black hole accretion flows directly scale across a factor of $\sim 10^8$ in black hole mass and across different accretion states. Using Ruan et al. (2019) as a guide, there are potentially three accretion regimes: (1) a "High/Soft State" with $\eta_{\rm Edd} \gtrsim -1$; (1) a "Low/Hard State" with $-2 \lesssim \eta_{\rm Edd} \lesssim -1$; (1) a "Low/Hard State" with $\eta_{\rm Edd} \lesssim -2$. These are given as shaded regions in Figure 7.

While we note there is interest in plotting these accretion rates, and motivation from Noda & Done (2018) and Ruan et al. (2019), we very much caution on over-interpretation at this juncture. The point of this paper was to report on three very interesting CLQs. Our object definitions are based on empirical, observed properties. We are not suggesting that CSQs/CLQs are similar to the X-ray binary models. The potential for physical connections of accretion physics across the large-range of mass-scales is tantalising. But is left to future investigations.

5 CONCLUSIONS

In this paper we have reported on three redshift $z > 2$ quasars with dramatic changes in their C IV emission lines, the first 'Changing-Look" quasars at high redshift. This is also the first time the changing-look behaviour has been seen in a high-ionisation emission line.

- SDSS J1205+3422, J1638+2827 and J2228+2201 show interesting behaviour in their observed optical light curves, and subsequent spectroscopy shows significant changes in the C IV broad emission line, with both line collapse and emergence being displayed in rest-frame timescales of ~240-1640 days.
- Where observed, the profile of the Lyα/N V emission complex also changes, and there is tentative evidence for changes in the Mg II line.
- Although line measurements from the three quasars show large changes in the C IV line flux-line width plane, the quasars are not seen to be outliers when considered against the full $z > 2$ quasar population in terms of (rest) Equivalent Width and FWHM properties.
- We put these observations in context with recent "state-change" models, but note that even in their 'low-state', the C IV CLQs are above ~ 10% in Eddington luminosity.

Availability of Data and computer analysis codes

All materials, databases, data tables and code are fully available at: `https://github.com/d80b2t/CIV_CLQs`.

ACKNOWLEDGEMENTS

NPR acknowledges support from the STFC and the Ernest Rutherford Fellowship scheme. MJG is supported in part by the NSF grants AST-1815034, and the NASA grant 16-ADAP16-0232.

We thank:

∘ Andy Lawrence, Mike Hawkins and David Homan for useful discussion.

This paper heavily used TOPCAT (v4.4) (Taylor 2005, 2011). This research made use of `Astropy`, a community-developed core Python package for Astronomy (Astropy Collaboration et al. 2013; The Astropy Collaboration et al. 2018).

Funding for SDSS-III has been provided by the Alfred P. Sloan Foundation, the Participating Institutions, the National Science Foundation, and the U.S. Department of Energy Office of Science. The SDSS-III web site is http://www.sdss3.org/. SDSS-III is managed by the Astrophysical Research Consortium for the Participating Institutions of the SDSS-III Collaboration including the University of Arizona, the Brazilian Participation Group, Brookhaven

National Laboratory, Carnegie Mellon University, University of Florida, the French Participation Group, the German Participation Group, Harvard University, the Instituto de Astrofisica de Canarias, the Michigan State/Notre Dame/JINA Participation Group, Johns Hopkins University, Lawrence Berkeley National Laboratory, Max Planck Institute for Astrophysics, Max Planck Institute for Extraterrestrial Physics, New Mexico State University, New York University, Ohio State University, Pennsylvania State University, University of Portsmouth, Princeton University, the Spanish Participation Group, University of Tokyo, University of Utah, Vanderbilt University, University of Virginia, University of Washington, and Yale University.

This publication makes use of data products from the Wide-field Infrared Survey Explorer, which is a joint project of the University of California, Los Angeles, and the Jet Propulsion Laboratory/California Institute of Technology, and NEOWISE, which is a project of the Jet Propulsion Laboratory/California Institute of Technology. WISE and NEOWISE are funded by the National Aeronautics and Space Administration.

REFERENCES

Abazajian K. N., et al., 2009a, ApJS, 182, 543
Abazajian K. N., et al., 2009b, ApJS, 182, 543
Abolfathi et al., 2018, ApJS, 235, 42
Abramowicz M. A., Czerny B., Lasota J. P., Szuszkiewicz E., 1988, ApJ, 332, 646
Alam S., et al., 2015, ApJS, 219, 12
Alloin D., Pelat D., Phillips M., Whittle M., 1985, ApJ, 288, 205
Antonucci R., 2018, Nature Astronomy, 2, 504
Astropy Collaboration et al., 2013, Astron. & Astrophys., 558, A33
Baldwin J. A., 1977, ApJ, 214, 679
Bellm E. C., et al., 2019a, PASP, 131, 018002
Bellm E. C., et al., 2019b, PASP, 131, 068003
Bian W.-H., Fang L.-L., Huang K.-L., Wang J.-M., 2012, MNRAS, 427, 2881
Calderone G., et al., 2017, MNRAS, 472, 4051
Cutri R. M. o., 2013, Technical report, Explanatory Supplement to the AllWISE Data Release Products. IPAC/Caltech
Cutri R. M., et al., 2011, Technical report, Explanatory Supplement to the WISE Preliminary Data Release Products. IPAC/Caltech
Dawson K., et al., 2013, AJ, 145, 10
Dawson K. S., Kneib J.-P., et al., 2016, AJ, 151, 44
Dexter J., Agol E., 2011, ApJ Lett., 727, L24
Doan A. N., et al., 2019, in American Astronomical Society Meeting Abstracts #233. p. 242.23
Drake A. J., et al., 2009, ApJ, 696, 870
Drake A. J., et al., 2013, ApJ, 763, 32
Dyer J. C., Dawson K. S., du Mas des Bourboux H., Vivek M., Bizyaev D., Oravetz A., Pan K., Schneider D. P., 2019, ApJ, 880, 78
Eisenstein D. J., Weinberg D. H., et al., 2011, AJ, 142, 72
Elvis M., 2000, ApJ, 545, 63
Fukugita M., Ichikawa T., Gunn J. E., Doi M., Shimasaku K., Schneider D. P., 1996, AJ, 111, 1748
Goad M. R., Korista K. T., Knigge C., 2004, MNRAS, 352, 277
Graham M. J., Djorgovski S. G., Drake A. J., Mahabal A. A., Chang M., Stern D., Donalek C., Glikman E., 2014, MNRAS, 439, 703
Graham M. J., et al., 2015a, MNRAS, 453, 1562
Graham M. J., et al., 2015b, Nat, 518, 74
Graham M. J., Djorgovski S. G., Drake A. J., Stern D., Mahabal A. A., Glikman E., Larson S., Christensen E., 2017, MNRAS, 470, 4112
Graham M. J., et al., 2019a, arXiv e-prints, p. arXiv:1905.02262
Graham M. J., et al., 2019b, PASP, 131, 078001
Guo H., Sun M., Liu X., Wang T., Kong M., Wang S., Sheng Z., He Z., 2019, ApJ Lett., 883, L44
Hamann F., Ferland G., 1999, ARA&A, 37, 487
Hamann F., et al., 2017, MNRAS, 464, 3431
Hemler Z. S., et al., 2019, ApJ, 872, 21
Homan D., Macleod C. L., Lawrence A., Ross N. P., Bruce A., 2019, arXiv e-prints, p. arXiv:1910.11364
Hutchinson T. A., et al., 2016, AJ, 152, 205
Jensen T. W., et al., 2016, ApJ, 833, 199
Kaiser N., et al., 2010, in Society of Photo-Optical Instrumentation Engineers (SPIE). p. 0, doi:10.1117/12.859188
Kozłowski S., 2017, ApJS, 228, 9
Kramida A., Ralchenko Y., Reader J., NIST ASD Team 2018, doi:10.18434/T4W30F,
Kramida A., Yu. Ralchenko Reader J., and NIST ASD Team 2019, NIST Atomic Spectra Database (ver. 5.7.1), [Online]. Available: `https://physics.nist.gov/asd` [2019, November 7]. National Institute of Standards and Technology, Gaithersburg, MD.
LaMassa S. M., et al., 2015, ApJ, 800, 144
Lawrence A., 2018, Nature Astronomy, 2, 102
Leighly K. M., 2004, ApJ, 611, 125
Lightman A. P., Eardley D. M., 1974, ApJ Lett., 187, L1
MacLeod C. L., et al., 2012, ApJ, 753, 106
MacLeod C. L., et al., 2019, ApJ, 874, 8
Magnier E. A., et al., 2013, ApJS, 205, 20
Mahabal A. A., et al., 2011, Bulletin of the Astronomical Society of India, 39, 387
Mainzer A., et al., 2011, ApJ, 731, 53
Margala D., Kirkby D., Dawson K., Bailey S., Blanton M., Schneider D. P., 2016, ApJ, 831, 157
Masci F. J., et al., 2019, PASP, 131, 018003
Matthews T. A., Sandage A. R., 1963, ApJ, 138, 30
McKernan B., Ford K. E. S., Kocsis B., Lyra W., Winter L. M., 2014, MNRAS, 441, 900
McKernan B., et al., 2018, ApJ, 866, 66
Meyer R. A., Bosman S. E. I., Ellis R. S., 2019, MNRAS, 487, 3305
Murray N., Chiang J., Grossman S. A., Voit G. M., 1995, ApJ, 451, 498
Myers A. D., et al., 2015, ApJS, 221, 27
Noda H., Done C., 2018, MNRAS, 480, 3898
Oke J. B., Gunn J. E., 1983, ApJ, 266, 713
Oke J. B., et al., 1995, PASP, 107, 375
Pâris I., Petitjean P., Ross N. P., et al., 2017, Astron. & Astrophys., 597, A79
Pâris I., et al., 2018, Astron. & Astrophys.
Pogge R. W., Peterson B. M., 1992, AJ, 103, 1084
Proga D., Stone J. M., Kallman T. R., 2000, ApJ, 543, 686
Rakić N., La Mura G., Ilić D., Shapovalova A. I., Kollatschny W., Rafanelli P., Popović L. Č., 2017, Astron. & Astrophys., 603, A49
Richards G. T., et al., 2002, AJ, 123, 2945
Richards G. T., et al., 2011, AJ, 141, 167
Ross N. P., et al., 2012, ApJS, 199, 3
Ross N. P., et al., 2015, MNRAS, 453, 3932
Ross N. P., et al., 2018, MNRAS, 480, 4468
Ruan J. J., Anderson S. F., Eracleous M., Green P. J., Haggard D., MacLeod C. L., Runnoe J. C., Sobolewska M. A., 2019, arXiv e-prints, p. arXiv:1903.02553v1
Schneider D. P., et al., 2010, AJ, 139, 2360
Shakura N. I., Sunyaev R. A., 1973, Astron. & Astrophys., 24, 337
Shen Y., et al., 2011, ApJS, 194, 45
Shen Y., et al., 2015, ApJS, 216, 4
Shen Y., et al., 2019, ApJS, 241, 34
Shields J. C., 2007, in Ho L. C., Wang J. W., eds, Astronomical Society of the Pacific Conference Series Vol. 373, The Central Engine of Active Galactic Nuclei. p. 355 (`arXiv:astro-ph/0612613`)
Smee S. A., et al., 2013, AJ, 146, 32
Stern D., et al., 2018, ApJ, submitted
Stoughton C., et al., 2002, AJ, 123, 485
Stubbs C. W., et al., 2010, ApJS, 191, 376
Sun M., Xue Y., Richards G. T., Trump J. R., Shen Y., Brandt W. N., Schneider D. P., 2018, ApJ, 854, 128
Taylor M. B., 2005, in Shopbell P., Britton M., Ebert R., eds, Astronomical

Society of the Pacific Conference Series Vol. 347, Astronomical Data Analysis Software and Systems XIV. p. 29
Taylor M., 2011, TOPCAT: Tool for OPerations on Catalogues And Tables, Astrophysics Source Code Library (ascl:1101.010)
The Astropy Collaboration et al., 2018, preprint, (arXiv:1801.02634v2)
Tonry J. L., et al., 2012, ApJ, 750, 99
Trakhtenbrot B., et al., 2019, ApJ, 883, 94
Wilhite B. C., Vanden Berk D. E., Brunner R. J., Brinkmann J. V., 2006, ApJ, 641, 78
Wright E. L., et al., 2010, AJ, 140, 1868
York D. G., et al., 2000, AJ, 120, 1579
Zakamska N. L., et al., 2016, MNRAS, 459, 3144
Zakamska N. L., et al., 2019, MNRAS, 489, 497

This paper has been typeset from a TEX/LATEX file prepared by the author.